The Astrophysical Journal, 888:14 (11pp), 2020 January 1 https://doi.org/10.3847/1538-4357/ab58cd

# Resolving 3D Disk Orientation Using High-resolution Images: New Constraints on Circumgalactic Gas Inflows

Stephanie H. Ho[1,2,3] and Crystal L. Martin[3]
[1] George P. and Cynthia Woods Mitchell Institute for Fundamental Physics and Astronomy, Texas A&M University, College Station, TX 77843-4242, USA
shho@physics.tamu.edu
[2] Department of Physics and Astronomy, Texas A&M University, College Station, TX 77843-4242, USA; cmartin@physics.ucsb.edu
[3] Department of Physics, University of California, Santa Barbara, CA 93106, USA

*Received 2019 January 30; revised 2019 November 13; accepted 2019 November 17; published 2019 December 30*

## Abstract

We constrain gas inflow speeds in star-forming galaxies with color gradients consistent with inside-out disk growth. Our method combines new measurements of disk orientation with previously described circumgalactic absorption in background quasar spectra. Two quantities, a position angle and an axis ratio, describe the projected shape of each galactic disk on the sky, leaving an ambiguity about which side of the minor axis is tipped toward the observer. This degeneracy regarding the 3D orientation of disks has compromised previous efforts to measure gas inflow speeds. We present *Hubble Space Telescope* and Keck/LGSAO imaging that resolves the spiral structure in five galaxies at redshift $z \approx 0.2$. We determine the sign of the disk inclination for four galaxies, under the assumption that spiral arms trail the rotation. We project models for both radial infall in the disk plane and circular orbits onto each quasar sightline. We compare the resulting line-of-sight velocities to the observed velocity range of Mg II absorption in spectra of background quasars, which intersect the disk plane at radii between 69 and 115 kpc. For two sightlines, we constrain the maximum radial inflow speeds as 30–40 km s$^{-1}$. We also rule out a velocity component from radial inflow in one sightline, suggesting that the structures feeding gas to these growing disks do not have unity covering factor. We recommend appropriate selection criteria for building larger samples of galaxy–quasar pairs that produce orientations sensitive to constraining inflow properties.

*Unified Astronomy Thesaurus concepts:* Quasar absorption line spectroscopy (1317); Laser guide stars (904); Extragalactic astronomy (506); Circumgalactic medium (1879); Galaxy evolution (594); Galaxy formation (595)

## 1. Introduction

Gas accretion onto galaxies shapes the growth of their disks. Decades of observations have demonstrated that galaxies need a continuous gas supply to explain the star formation history and the stellar metallicity distribution of the disks. Without a continuous gas supply, the gas reservoir around galaxies will exhaust within a few gigayears, and the galaxies cannot sustain their star formation rates (Bigiel et al. 2008, 2011; Leroy et al. 2008, 2013; Rahman et al. 2012). The accreting gas will thereby prolong the gas consumption time (Kennicutt 1983) and explain the color of galaxy disks along the Hubble sequence (Kennicutt 1998). The infall of metal-poor gas also explains the relative paucity of low metallicity stars in the disk, known as the G-dwarf problem in the solar neighborhood (van den Bergh 1962; Schmidt 1963; Sommer-Larsen 1991) but not unique to the Milky Way (Worthey et al. 1996).

In hydrodynamical simulations, galaxies accrete cooling gas to grow the galactic disks (Oppenheimer et al. 2010; Brook et al. 2012; Shen et al. 2012; Ford et al. 2014; Christensen et al. 2016). The torques generated by the disk align the cooling, infalling gas with the preexisting disk (Danovich et al. 2012, 2015). The newly accreted gas then forms an extended cold flow disk that corotates with the central disk (Stewart et al. 2011, 2013, 2017). Because gas accreted at later times has higher angular momentum, the late time infall builds the disk inside-out (Kimm et al. 2011; Pichon et al. 2011; Lagos et al. 2017; El-Badry et al. 2018).

Direct observations of gas accretion onto galaxies remain sparse (Putman et al. 2012). Nevertheless, recent studies of the circumgalactic medium (CGM) through quasar sightlines have shed light on detecting the inflowing gas. The CGM extends to the galaxy virial radii (Tumlinson et al. 2017) and contains a significant fraction of the baryonic mass associated with the galaxy halos (Werk et al. 2014). For the low-ionization-state gas (e.g., Mg$^+$) detected as intervening absorption in quasar sightlines, absorption near the galaxy major and minor axes is often explained by inflows and outflows (e.g., Bouché et al. 2012; Kacprzak et al. 2012, 2015; Nielsen et al. 2015); minor- and major-axis sightlines intersect winds blown out perpendicular to the disk plane and gas accreted near the disk plane, respectively (Shen et al. 2012). In addition, Martin et al. (2019, hereafter M19) studied the circumgalactic gas kinematics of a sample of 50 $z \approx 0.2$ blue galaxies, and the galaxies have quasar sightlines intersecting the inner CGM at all azimuthal angles.[4] They found that the Mg II absorption strength increases with the velocity range, both of which increase toward the minor axis. They concluded that minor-axis sightlines intersect the CGM kinematically disturbed by galactic outflows, a property that has been shown for galaxies that are undergoing or have recently undergone a strong starburst (Heckman et al. 2017).

Ho et al. (2017, hereafter Paper I) studied a subset of 15 galaxy–quasar pairs from M19, and all 15 quasar sightlines lie within 30° from the galaxy major axes. In 13 out of the 15 major-axis sightlines, Ho et al. detected Mg II absorption, and the Mg II Doppler shift shares the same sign as the galactic disk rotation at the quasar side of the galaxy. This implies that the Mg II gas in the inner CGM corotates with the galaxy disk.

---

[4] We define the azimuthal angle as the angle between the galaxy major axis and the line joining the quasar and the galaxy center.

**$i > 0$** View the disk from the bottom

**$i < 0$** View the disk from the top

**Figure 1.** Sign of disk inclination. For a measured disk axis ratio, the disk can tilt in two different ways with respect the plane of the sky. From the perspective of the observer, switching the sign of disk inclination flips the near side and the far side of the galaxy disk.

Moreover, M19 found no net counter-rotating Mg II systems within 45° of the major axis. Therefore, these results have strengthened previous results from smaller, diverse galaxy samples that also found corotating low-ionization-state gas in major-axis sightlines (Steidel et al. 2002; Kacprzak et al. 2010; Bouché et al. 2013, 2016; Zabl et al. 2019), a property that also describes Ly$\alpha$ absorbers (Barcons et al. 1995; Prochaska & Wolfe 1997; Chen et al. 2005).

To explain the kinematics of the Mg II absorbing gas, Paper I explored simple models to describe the velocity range spanned by the absorption. We have adopted disk models, instead of rotating halo models, as the simplest configuration. This is motivated in part by hydrodynamic simulations that show the corotation between the central disks and the extended cold gas disks (e.g., Stewart et al. 2011; El-Badry et al. 2018). Previous observational work has also attempted to model the Doppler shifts and/or velocity ranges of Ly$\alpha$ and Mg II absorption systems with disk rotation (e.g., Mg II in Steidel et al. 2002 and Kacprzak et al. 2010, 2011, and Ly$\alpha$ in Barcons et al. 1995; Prochaska & Wolfe 1997; Chen et al. 2005). It is well known that thin, rotating disks fail to reproduce the broad velocity range of absorption systems. A wider velocity range is produced by thick disks (cylinders), a lag in rotation (i.e., a vertical velocity gradient), radial inflow on the disk plane, or a combination of these options (Steidel et al. 2002; Kacprzak et al. 2010, 2011; Paper I). We have selected major-axis sightlines that intersect the inner CGM of galaxies with inclined disks. If the gas disks extend beyond the visible disks of galaxies, then our sightlines will intersect gas near the extended disk planes within half the virial radii. Therefore, motivated by previous work and our selection of major-axis sightlines, we adopt a disk geometry and explore the consequences for the gas dynamics.

With a disk geometry, the modeled line-of-sight (LOS) velocity depends on the galaxy disk orientation in 3D space. In addition to the disk axis ratio and position angle, establishing the 3D disk orientation requires the sign of disk inclination. The sign of disk inclination indicates how the galaxy disk tilts with respect to the plane of the sky. From the perspective of the observer, switching the sign flips the near side and the far side of the galaxy disk; Figure 1 illustrates this concept. We have implemented this geometrical difference into our inflow model in Paper I. The model combines a tangential (rotation) and a radial (inflow) velocity component, producing gas spiraling inward on the disk plane. When the disk flips, the tangential and radial velocity components add together differently. This alters whether the radial inflow boosts or cancels the projected rotation velocity, resulting in different modeled LOS velocity ranges. We have explained the model in detail and demonstrated this asymmetry in the Appendix of Paper I.

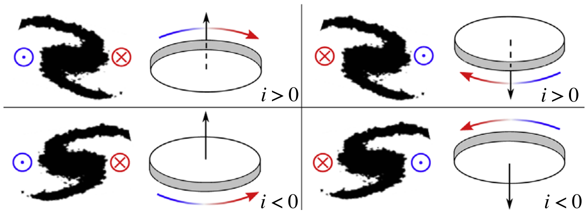

**Figure 2.** Deducing disk tilt from the wrapping direction of spiral arms and measured galaxy disk rotation. On each schematic diagram of the spiral arms, the blue dot and the red cross represent the blueshifted and the redshifted sides of the measured disk rotation. The deduced disk tilt is shown on the right. The curved color arrow indicates the rotation direction of each disk, and the straight black arrow shows the corresponding angular momentum vector.

In general, the asymmetry originates from velocity vectors added together differently when the disk flips. Through the simple radial inflow model, we will demonstrate the use of the disk tilt to constrain disk inflows. In M19, we have also discussed how the disk tilt constrains outflow models and explains minor-axis absorption. Hence, the disk tilt is an important parameter when modeling circumgalactic gas kinematics.

In this paper, we will demonstrate a method to independently deduce the disk tilt, i.e., the sign of disk inclination, a priori; Figure 2 illustrates this concept. Because disks rotate differentially, and only trailing spirals are long-lived (Carlberg & Freedman 1985), spiral arms generally trail the direction of rotation. Hence, using the observed wrapping direction of spiral arms and the direction of disk rotation measured from the rotation curve, we can determine which way the disk tilts on the sky.

This work examines five galaxy–quasar pairs from Paper I and M19. We present new, high-resolution images for the five galaxies, including optical images from the *Hubble Space Telescope* (*HST*) and adaptive-optics-corrected (AO-corrected), near-infrared images from the Keck Observatory. Section 2 briefly describes the imaging observations. Section 3 shows that these new images reveal the wrapping direction of the spiral arms for four galaxies. Together with the rotation curves (presented in Paper I), we determine how the disks tilt and examine whether/how the tilts constrain the radial inflow model in Paper I. Section 4 discusses the implications of our results, which we summarize in Section 5. Throughout the paper, we adopt the cosmology from Planck Collaboration et al. (2016), with $h = 0.6774$, $\Omega_m = 0.3089$, $\Omega_\Lambda = 0.6911$, and $\Omega_b = 0.0486$.

## 2. Data and Observations

We present new imaging observations of five galaxies from the galaxy–quasar pairs in Paper I and M19. For these five $z \approx 0.2$, blue galaxies, Paper I and M19 detected Mg II absorption along the quasar sightlines and measured the galaxy rotation curves using the Low Resolution Imaging Spectrometer (LRIS; Oke et al. 1995; Rockosi et al. 2010) at Keck and the Double Imaging Spectrograph at the Apache Point Observatory 3.5 m telescope.[5] Table 1 summarizes the key spectroscopic measurements of the five systems. This paper presents new optical images from *HST* Wide Field Camera 3 (WFC3) and/or AO-corrected, near-infrared images from the

---

[5] Instrument specifications can be found in the manual written by Robert Lupton, which is available at http://www.apo.nmsu.edu/35m_operations/35m_manual/Instruments/DIS/DIS_usage.html#Lupton_Manual.

**Table 1**
Target Information and Summary of Spectroscopic Measurements

| Quasar Name<br>(1) | Galaxy Name<br>(2) | $i$ (°)<br>(3) | $\alpha$ (°)<br>(4) | $z_{\mathrm{gal}}$<br>(5) | $b$ (kpc)<br>(6) | $R_g$ (kpc)<br>(7) | $W_r^{2796}$ (Å)<br>(8) | $v_D^{\mathrm{Mg\ II}}$ (km s$^{-1}$)<br>(9) | $\Delta v_{2796}$ (km s$^{-1}$)<br>(10) | $\Delta v_{2796}^{\mathrm{intr}}$ (km s$^{-1}$)<br>(11) | $v_{\mathrm{rot}}$ (km s$^{-1}$)<br>(12) |
|---|---|---|---|---|---|---|---|---|---|---|---|
| J091954+291408 | J091954+291345 | 73 | 15 | 0.23288 | 88 | 115 | $0.52^{+0.02}_{-0.02}$ | 137 ± 4 | [−51, 292] | [7, 235] | 250 |
| | | | | | | | $0.22^{+0.01}_{-0.01}$ | −154 ± 9 | [−266, −8] | [−208, −66] | [a] |
| J102907+421752 | J102907+421737 | 50 | 19 | 0.26238 | 65 | 69 | $0.12^{+0.03}_{-0.03}$ | −53 ± 15 | [−134, 34] | [−76, −24] | 155 |
| J123049+071036 | J123049+071050 | 38 | 4 | 0.39946 | 98 | 98 | $0.08^{+0.02}_{-0.01}$ | −91 ± 34[b] | [−172, −21] | [−115, −79] | 190 |
| J124601+173156 | J124601+173152 | 63 | 11 | 0.26897 | 19 | 20 | $0.31^{+0.03}_{-0.03}$ | −299 ± 11 | [−404, −200] | [−314, −290] | 60 |
| J142501+382100 | J142459+382113 | 61 | 8 | 0.21295 | 83 | 85 | $0.24^{+0.03}_{-0.02}$ | 9 ± 7 | [−128, 221] | [−37, 130] | 190 |

**Notes.** (1) Name of the quasar. (2) Name of the galaxy. (3) Inclination of the galactic disk. (4) Azimuthal angle, the angle between the galaxy major axis and the quasar sightline. (5) Galaxy systemic redshift measured from emission lines. (6) Sightline impact parameter. (7) Galactocentric radius. (8) Rest-frame equivalent width of Mg IIλ2796. (9) Mg II Doppler shift measured from line profile fitting. (10) Measured velocity range. (11) Intrinsic velocity range (corrected for the line broadening effect due to the instrumental resolution). (12) Asymptotic galaxy rotation speed.

[a] We attribute this blue, weak absorption component to a red galaxy within the group. See Paper I or Section 2.3 for details.

[b] The absorption system falls in a part of the LRIS spectrum without arc lamp lines. The dispersion solution is extrapolated about 200 Å beyond the last arc line, introducting potential systematic error.

**Table 2**
Imaging Observations

| Target Galaxy | Instrument | Exposure Time (s) | Filter | Field-of-view (″) | Plate Scale (″pixel$^{-1}$) | PSF FWHM[a] (″) | Observing Dates |
|---|---|---|---|---|---|---|---|
| J091954+291345 | Keck/NIRC2 | 600 | $K_s$ | 40″ × 40″ | 0.039686 | 0.20 | 2017 Jan 28 |
| J102907+421737 | *HST*/WFC3 UVIS | 1716 | F390W | 162″ × 162″[b] | 0.04 | 0.07 | 2017 Jan 25 |
| | *HST*/WFC3 UVIS | 700 | F814W | 162″ × 162″[b] | 0.04 | 0.07 | 2017 Jan 25 |
| | Keck/NIRC2 | 600 | $K_s$ | 40″ × 40″ | 0.039686 | 0.15 | 2017 Jan 26 |
| J123049+071050 | Keck/NIRC2 | 600 | $K_s$ | 40″ × 40″ | 0.04 | 0.12 | 2015 May 6 |
| J124601+173152 | *HST*/WFC3 UVIS | 1629 | F390W | 162″ × 162″[b] | 0.04 | 0.07 | 2017 Jan 28 |
| | *HST*/WFC3 UVIS | 700 | F814W | 162″ × 162″[b] | 0.04 | 0.07 | 2017 Jan 28 |
| | Keck/NIRC2 | 600 | $K_s$ | 40″ × 40″ | 0.039686 | 0.23 | 2017 Jan 26 |
| | Keck/NIRC2 | 1200 | $K_s$ | 40″ × 40″ | 0.039686 | 0.31 | 2017 Apr 13 |
| J142459+382113 | *HST*/WFC3 UVIS | 1674 | F390W | 162″ × 162″[b] | 0.04 | 0.07 | 2017 Jun 5 |
| | *HST*/WFC3 UVIS | 700 | F814W | 162″ × 162″[b] | 0.04 | 0.07 | 2017 Jun 5 |
| | Keck/NIRC2 | 600 | $K_s$ | 40″ × 40″ | 0.039686 | 0.14 | 2015 May 6 |

**Notes.**

[a] The FWHM of the point-spread function (PSF).

[b] The WFC3/UVIS channel has a rhomboidal field of view.

Keck NIRC2 camera of the galaxies. These high-resolution images reveal galaxy structural features that cannot be recognized in the Sloan Digital Sky Survey (SDSS) images, e.g., the wrapping of spiral arms, the presence of companion galaxies, etc. Table 2 lists the imaging observations of the galaxies. We describe the *HST* WFC3 and Keck NIRC2 observations in Sections 2.1 and 2.2, respectively. Section 2.3 briefly describes the environment of the galaxies.

### 2.1. HST WFC3 Observations

We imaged three galaxies using the WFC3/UVIS channel and the F390W and F814W broadband filters (Cycle 24, PID: 14754, PI: C. L. Martin). We list the exposure time for each galaxy in Table 2. The table also includes the field of view, the plate scale, and the FWHM of the point-spread function (PSF) of the UVIS channel.

Individual data frames were retrieved from MAST.[6] These data frames were already reduced and calibrated by the standard WFC3 calibration pipeline `calwf3`.[7] For the F390W data frames, we drizzled the three dithered images of each target using `DrizzlePac` (Fruchter et al. 2010).[8] But for the F814W data frames, because we only took two exposures per target, cosmic ray removal during drizzling was suboptimal. Therefore, we used L.A.Cosmic (van Dokkum 2001) to remove the cosmic rays from individual F814W frames. Then we drizzled the cleaned frames to produce the science images for individual targets.

### 2.2. Keck NIRC2 Observations

We observed all five galaxies with the NIRC2 camera on the Keck II telescope, using the paired quasar as the tip-tilt reference for the Keck laser guide star adaptive-optics system (LGSAO; van Dam et al. 2006; Wizinowich et al. 2006). M19 described the observation and the data reduction in detail. In

---

[6] http://archive.stsci.edu

[7] Documentation of `calwf3` can be found at Gennaro, M., et al. 2018, WFC3 Data Handbook, Version 4.0, (Baltimore: STScI).

[8] Documentation of `DrizzlePac` can be found at Gonzaga et al. (2012).

brief, we observed each galaxy using the $K_s$ broadband filter, which centered at 2.146 $\mu$m; Table 2 lists the $K_s$ observation. We reduced the images using the data reduction pipeline provided by the UCLA/Galactic center group (Ghez et al. 2008). The final images were dark corrected, flat-fielded, sky subtracted, and corrected for geometrical distortion.

### 2.3. Galaxy Environment

Galaxy group environment affects the properties of Mg II absorption, such as the absorption strength and velocity dispersion (Bordoloi et al. 2011; Johnson et al. 2015; Nielsen et al. 2018), and possibly leads to uncertain host galaxy assignment of the Mg II absorption. We have flagged three of the five target galaxies as potential group members (Paper I; M19).

J124601+173152 is in a rich environment, with three brighter galaxies having consistent photometric redshifts. While our target galaxy is the closest to the quasar sightline, both Paper I and M19 flagged this system because the host identification for the Mg II absorption may not be unique.

Because we lack spectroscopic redshifts for all but the closeset galaxies in our fields, we cannot classify the environment of the absorbers as Chen & Mulchaey (2009) and Johnson et al. (2013) did. Nevertheless, we searched for potential group members using the SDSS images and photometric redshifts of the galaxies in each field, and we found two other target galaxies potentially in groups. We found there is a potential group member near the target galaxy J102907+421737. Because our target is three times closer to the sightline than the other bright galaxy in the field, the association of Mg II absorption in the J102907+421752 sightline with our target galaxy is secure. Another target galaxy, J091954+291345, potentially forms a group with two red galaxies $4''.4$ and $8''.7$ away, both of which have photometric redshifts consistent with our target. The spectrum of our paired quasar detects two absorption systems. Following Paper I and M19, we assign the stronger system to the blue galaxy (our target), and we consider the weaker system as potentially not produced by our target.

## 3. Individual Galaxies: Disk Tilt and Gas Kinematic Modeling

The new, high-resolution images reveal the spiral structures for four of the five galaxies. We deduce how these disks tilt, and then we explore how their tilts constrain the gas kinematic modeling, which aims to explain the broad Mg II velocity range measured. Section 3.1 shows the new images and discusses the image processing steps. Section 3.2 reviews the key components of the radial inflow model from Paper I. Then in Section 3.3, we discuss individual galaxies regarding how each disk tilts, and we explore how it combines with the inflow model in Paper I and affects the modeled inflow properties.

### 3.1. Deducing the Disk Tilt From High-resolution Images

Figure 3 shows the images of individual galaxies and the deduced 3D disk orientations. We rotate the galaxy images such that each galaxy major axis aligns with the image $x$-axis, and the quasar sightline lies in the positive $x$-direction. Each schematic diagram in the last column illustrates the wrapping direction of spiral arms and direction of the disk rotation (curved, blue/red arrow). Following the concept illustrated by Figure 2 and the definition in M19, we deduce the sign of disk inclination, i.e., which way the disk tilts.

Contrasting our high-resolution images with the color images from the SDSS in Figure 3 highlights the resolving power of our new images. For the SDSS images, the median FWHM of the PSF in the $r$-band is $1''.3$. This is an order of magnitude higher than that for both WFC3 optical and the NIRC2 $K_s$ images. Therefore, these images accentuate the capability of the high-resolution imaging to reveal structures and companion galaxies that low-resolution imaging fails to resolve.

When the spiral arms are not prominent in the high-resolution images, we apply additional image processing steps to visually enhance the structural features. We create three-color images for J102907+421737, J124601+173152, and J142459+382113, all of which are observed in F390W, F814W, and $K_s$ bands (Figure 4). We use blue, green, and red colors to represent the three bands respectively.[9] The color images also allow us to visualize the spatial distribution of different stellar populations. In addition, the F390W image of J102907+421737 and the $K_s$ image of J123049+071050 only show weak traces of spiral arms. So, we process the images as follows to enhance the spiral features. First, we use GALFIT (Peng et al. 2002) to model the smooth galaxy emission component with an exponential disk surface brightness (SB) profile and convolve the model with the instrumental PSF. We model the instrumental PSF of the *HST* WFC3 using Tiny Tim (Krist et al. 2011), and for the $K_s$ image, we fit a Moffat profile to our paired quasar. The residual image, i.e., the difference between the original image and the convolved galaxy SB model, shows traces of spiral arms. Then, we apply a median filter to the residual and add it to the original F390W or $K_s$ images. For J102907+421737, we use the enhanced F390W image to create the three-color image. We present the processed images under the "Processed/Color Image" column in Figure 3.

### 3.2. Brief Description of the Disk Model and Radial Inflow

The simple inflow model in Paper I combines the tangential (rotational) and radial (inflow) velocity components on the disk plane. For the radial inflow component, we adopt a constant radial velocity,

$$\boldsymbol{v}_R(R, z) = v_R \hat{\boldsymbol{R}} , \tag{1}$$

where $v_R < 0$ for inflow. We model the rotation component as

$$\boldsymbol{v}_\phi(z) = v_{\rm rot} \exp(-|z|/h_v) \hat{\boldsymbol{\phi}} , \tag{2}$$

where $v_{\rm rot}$ represents the asymptotic galaxy rotation speed measured, and the velocity scale height $h_v$ introduces a vertical velocity gradient to create a rotational lag above and below the disk midplane. Paper I discussed two cases: (1) $h_v \rightarrow \infty$, i.e., without a velocity gradient, and (2) a fiducial $h_v$ value of 10 kpc, which produced vertical velocity gradients of 11 to 26 km s$^{-1}$ per kiloparsec for the galaxy sample. Because the fiducial 10 kpc value creates velocity gradients consistent with measurements of extraplanar gas, we follow Paper I and adopt the same fiducial $h_v$ value when we consider disks with lagging

---

[9] We register the images before creating the color images. We resample the pixels to the pixel scale of the WFC3 images and align all images using reference point sources in the common field.

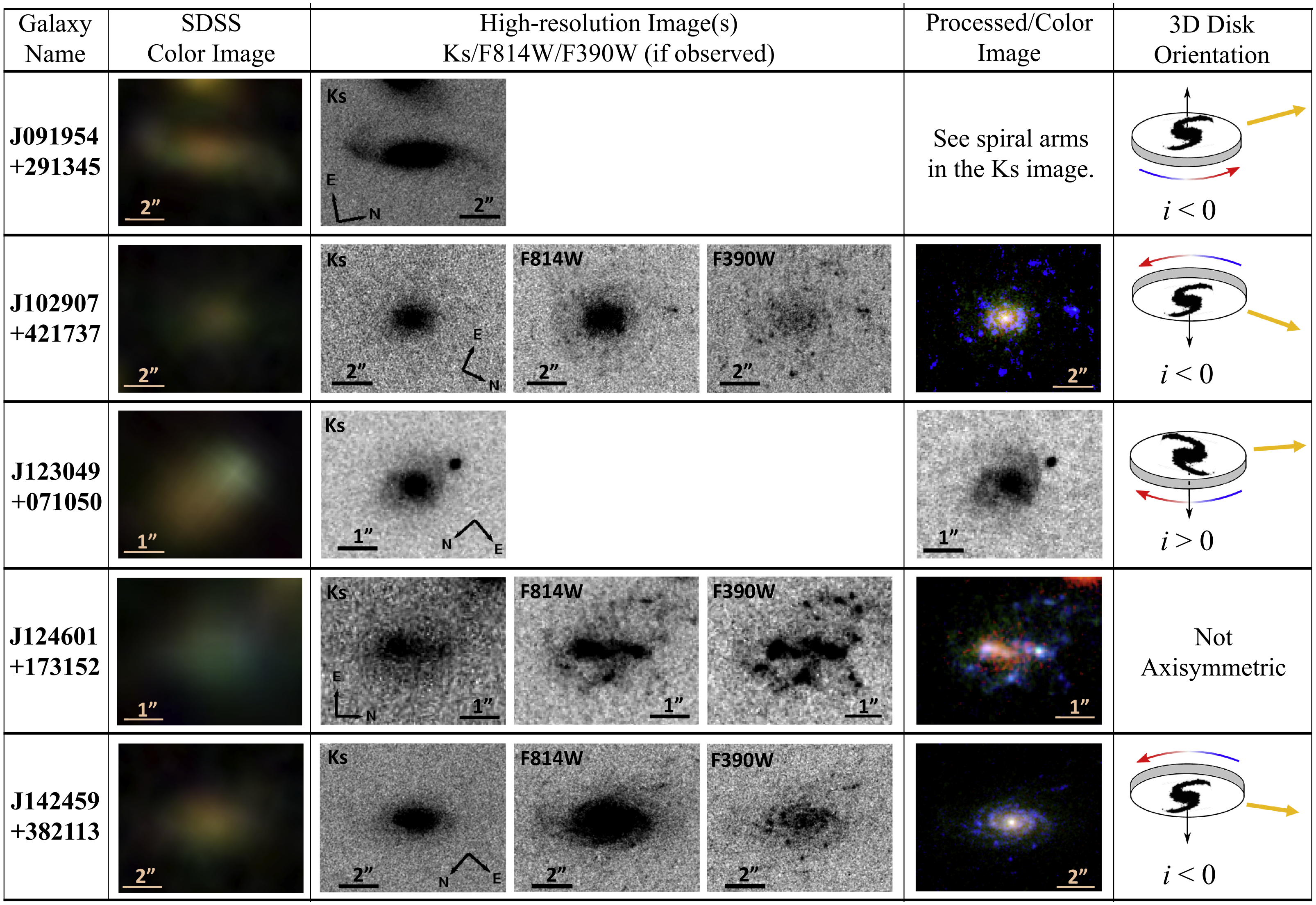

**Figure 3.** High-resolution galaxy images and the deduced 3D disk orientations. Each row corresponds to one galaxy, and column 1 shows the galaxy name. Column 2 demonstrates that the low-resolution SDSS images cannot resolve the galaxy structural features. Column 3 shows the high-resolution NIRC2 $K_s$, WFC3 F814W, and WFC3 F390W (if observed) for individual galaxies. For galaxies with spiral arms or structures that can hardly be distinguished in the original images, column 4 shows the processed images that visually enhanced the structural features. In particular, column 3 shows the three-color images for galaxies observed in all three bands. Column 5 illustrates the wrapping direction of the spiral arms, the measured disk rotation (the curved arrow), and the deduced 3D disk orientation. Each orange arrow points toward the direction of the quasar sightline. The images for individual galaxy have the same scale and the same orientation; each galaxy major axis aligns with the image *x*-axis, and the quasar sightline lies in the positive *x*-direction.

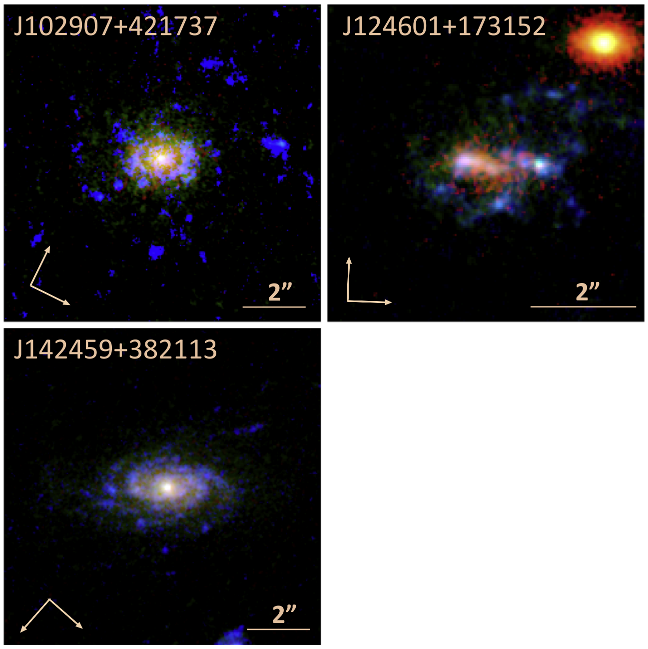

**Figure 4.** Composite F390W (blue), F814W (green), and $K_s$ (red) images. Both J102907+421737 and J142459+382113 show spiral arms and bluer outer disks. J124601+173152 shows two bright clumps along the N–S direction.

rotation. The velocity gradients have been measured to about 10 kpc vertically and over 20 kpc radially in nearby galaxies (Benjamin 2002; Oosterloo et al. 2007; Marasco & Fraternali 2011; Zschaechner et al. 2011, 2012; Gentile et al. 2013; Kamphuis et al. 2013), so our approach extrapolates into a regime unconstrained by direct measurements.

We obtain the LOS velocity $v_{\rm los}$ by taking the dot product between each of Equations (1) and (2) with the vector describing the quasar sightline. The impact parameter $b$ and azimuthal angle $\alpha$ set the orientation of the sightline with respect to the galaxy disk. The sign of the disk inclination $i$ describes which way the disk tilts, whereas the magnitude of the disk inclination and the modeled thickness $H_{\rm eff}$ (measured from the disk midplane) limit the pathlength along the sightline that intersects the disk. Along this sightline path, the bluest and the reddest ends of the $v_{\rm los}$ define the resultant LOS velocity range.

### 3.3. Disk Tilt of Individual Galaxies and Their Gas Kinematic Modeling

Using new individual galaxy images and the measured galaxy rotation curves (presented in Paper I), we determine which way the disk tilts. Then, we investigate whether and/or how the deduced disk tilt constrains the gas kinematic modeling and the inflow properties. Specifically, we explore whether the rotating disk model, without and with radial inflow, can reproduce the broad Mg II LOS velocity range measured along the quasar sightlines.

For individual galaxies, we show position–velocity (PV) diagrams, i.e., $D_{\rm los}$ versus $v_{\rm los}$, for the rotating-disk-only model (no radial inflow) and models with radial inflow for disks at $i > 0$ and $i < 0$. Contrasting the two tilts demonstrates how the a priori knowledge of the disk tilt affects the modeling. In each PV diagram, $D_{\rm los} = 0$ represents the disk midplane, and $D_{\rm los} < 0$ (>0) represents the sightline at the near (far) side of the disk. The cyan shaded region represents the measured LOS velocity range of the Mg II absorption. The cyan hashes indicate the uncertainties of the measured velocity range at the blue and red ends. The gray shaded region that enclosed the modeled $v_{\rm los}$ (black curve) shows the line broadening effect that matches the LRIS spectral resolution. The modeled LOS velocity range (gray shaded region) agrees with the measurement only if both the bluest and reddest ends of the modeled $v_{\rm los}$ fall within the uncertainties of the two ends of the measurement (cyan hashes). To illustrate the known problem that thin disks cannot explain broad velocity ranges, the two yellow markers in the PV diagram (left) indicate where the sightline intersects the boundary of an $H_{\rm eff} = 1$ kpc disk. Along the short sightline path that intersects the thin disk, because of the small variation in the LOS velocity, a thin disk can only produce a narrow velocity range.

#### 3.3.1. J091954+291345

The galaxy J091954+291345 clearly shows the spiral arms in the $K_s$ image. Together with the direction of disk rotation determined from the rotation curve, we deduce that the disk has a negative inclination.

A disk without a vertical velocity gradient can explain the over 300 km s$^{-1}$ LOS velocity range, but that would require a 500 kpc thick "disk" ($H_{\rm eff} = 250$ kpc) to match the blue absorption end. With $h_v = 10$ kpc, a significantly thinner disk of $H_{\rm eff} = 15$ kpc (left panel of Figure 5) can explain the same velocity range. Further reducing $H_{\rm eff}$ would make the absorption not blue enough to match the measurement. Considering also radial inflow for this $H_{\rm eff} = 15$ kpc disk, a positively inclined disk would allow an inflow speed of 140 km s$^{-1}$ before the absorption becomes too red at the disk midplane, but the disk would need to be thicker to match the blue absorption end (middle panel). On the other hand, a negatively inclined disk can reproduce the measured velocity range with radial inflow of no more than 30 km s$^{-1}$ (right panel); otherwise the absorption would not be red enough at the disk midplane. Because the two disk tilts permit significantly different radial inflow scenarios, the deduced negative disk inclination tightens the constraint on the radial inflow speed to at most 30 km s$^{-1}$.

#### 3.3.2. J102907+421737

For J102907+421737, the F390W image shows the spiral arms most clearly, and we visually enhance the spiral features and create the color image as described in Section 3.1. The color image also shows that the outer disk is bluer than the inner disk. This suggests that the outer disk is younger than the inner disk (de Jong 1996; Bell & de Jong 2000; MacArthur et al. 2004), indicating an inside-out disk growth. From the revealed wrapping direction of the spiral arms and the measured disk rotation, we deduce that the disk has a negative inclination.

A disk without a velocity gradient can explain the ~100 km s$^{-1}$ measured LOS velocity range. However, the disk would need an $H_{\rm eff}$ of 65 kpc to bring the absorption close to the galaxy systemic velocity in order to match the red absorption end. With $h_v = 10$ kpc, a thinner rotating disk of $H_{\rm eff} = 10$ kpc can reproduce the LOS velocity range of the absorption within measurement uncertainties (left panel of Figure 6). Further reducing the disk thickness would make the

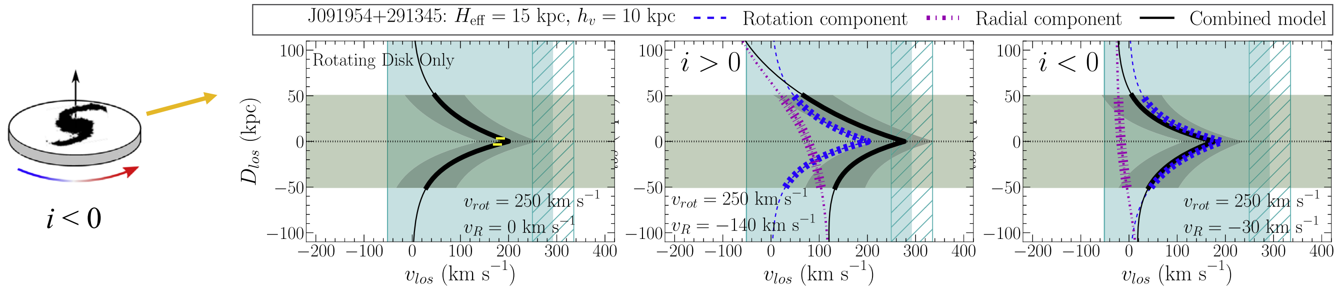

**Figure 5.** J091954+291345: disk tilt tightens constraint on radial inflow speed. The galaxy disk is negatively inclined (the schematic diagram and Section 3.3.1). A rotating disk of $H_{\rm eff} = 15$ kpc and $h_v = 10$ kpc can reproduce the LOS velocity range of the absorption (left), and a thinner disk cannot reproduce the blue absorption end. For example, the pathlength within an $H_{\rm eff} = 1$ kpc disk is short, producing only a narrow velocity range (yellow markers). Disks with positive (middle) and negative (right) inclinations allow maximum radial inflow speeds of 140 and 30 km s$^{-1}$ respectively. Otherwise, the absorption becomes too red or not red enough at the disk midplane. Hence, deducing the disk as negatively inclined limits the inflow speed to 30 km s$^{-1}$.

absorption not red enough to match with the measurement. If we also consider radial inflow on the $H_{\rm eff} = 10$ kpc disk, then the inflow speed for a positively (negatively) inclined disk cannot exceed 80 (40) km s$^{-1}$. Otherwise, the absorption becomes not blue enough (too blue) at the disk midplane; see the middle (right) panel. Hence, the inferred negative disk inclination limits the radial inflow speed to at most 40 km s$^{-1}$.

### 3.3.3. J123049+071050

The high-resolution $K_s$ image resolves the target "galaxy" into two objects: a galaxy with spiral arms and a possible satellite. The galaxy also has weak traces of spiral arms, and we visually enhance the arms as described in Section 3.1. From the wrapping direction of the spiral arms and the direction of disk rotation, we deduce that the disk has a positive inclination.

A rotating disk without a vertical velocity gradient can reproduce the 160 km s$^{-1}$ measured velocity range, but the "disk" has to be 260 kpc thick ($H_{\rm eff} = 130$ kpc) to bring the red absorption end close to the galaxy systemic velocity. In contrast, the fiducial model with a vertical velocity gradient only requires a 10 kpc thick disk ($H_{\rm eff} = 5$ kpc) to reproduce the velocity range spanned by the absorption (left panel of Figure 7).

Knowing the disk tilt a priori cannot rule out radial inflow nor constrain the radial inflow speed for this galaxy. Even as the inflow speed increases from 0 to 300 km s$^{-1}$, the LOS velocities at both the bluest and the reddest ends change by no more than 20 km s$^{-1}$ (middle and right panels of Figure 7). This 20 km s$^{-1}$ shift is allowed by the measurement uncertainties. This means that regardless of which way the disk tilts, an inflow speed as large as 300 km s$^{-1}$ can always explain the measured velocity range. The reason of why the LOS velocity is insensitive to both the radial inflow speed and the disk tilt is because of the low disk inclination ($i = 38°$) and small azimuthal angle ($\alpha = 4°$). Section 4 discusses how both factors affect the effectiveness of constraining the radial speed.

### 3.3.4. J124601+173152

Both F390W and F814W images of J124601+173152 reveal that the galaxy has an irregular, clumpy structure. In both F390W and F814W images, the galaxy shows two bright clumps along the N–S direction. However, the $K_s$ image only detects a single nucleus that lies at the location of the southern clump. The color image also shows that the emission in $K_s$ overlaps with the southern clump only.

Altogether, our images suggest that this galaxy has a complicated, clumpy structure instead of a typical, axisymmetric disk morphology. Hence, we do not define how this galaxy "disk" tilts, and we do not create disk models to explain the Mg II absorption.

### 3.3.5. J142459+382113

Both F390W and F814W images of J142459+382113 unambiguously detect the spiral arms. From the wrapping direction of the arms and the measured disk rotation, we deduce the disk as being negatively inclined.

Moreover, the color image clearly shows that the outer disk is bluer than the inner disk. The presence of the color gradient is also supported by the larger disk scalelengths measured at the bluer bands. The color gradient indicates that the outer disk has a younger stellar population and a lower metallicity than the inner disk, suggesting the disk grows inside-out. In Section 4, we will discuss the implications of this disk growing inside-out together with the result from our inflow modeling.

The Mg II absorption detected in the quasar sightline has a small Doppler shift. Since the broad velocity range spans both sides of the galaxy systemic velocity, neither the line broadening by instrumental resolution nor any structure with only rotation can explain the two-sided absorption. A rotating disk also produces bluer absorption than measured near the disk midplane. The left panel of Figure 8 illustrates this problem using a disk with a vertical velocity gradient. A disk without a velocity gradient makes the problem worse, because the absence of the gradient makes the projected rotation velocity peak at a higher velocity (i.e., bluer) along the LOS. Therefore, while the radial inflow model can produce two-sided absorption that a rotation-only structure fails to produce, solving the problem of excess blue absorption from the disk rotation requires the LOS velocities from the inflow and the rotation components to have opposite signs near the midplane.

Only a positively inclined disk can achieve this configuration. The middle panel of Figure 8 illustrates that the radial inflow (rotation) component creates a positive (negative) LOS velocity near the disk midplane, and reproducing the measured velocity range requires an $H_{\rm eff} = 10$ kpc disk with an exceptionally high radial inflow speed of 480 km s$^{-1}$. The problem is that we deduce the disk as being negatively inclined. Radial inflow makes the absorption even bluer than disk rotation alone, because both velocity components have the same Doppler sign near the midplane. The right panel illustrates this problem using a fiducial inflow speed of

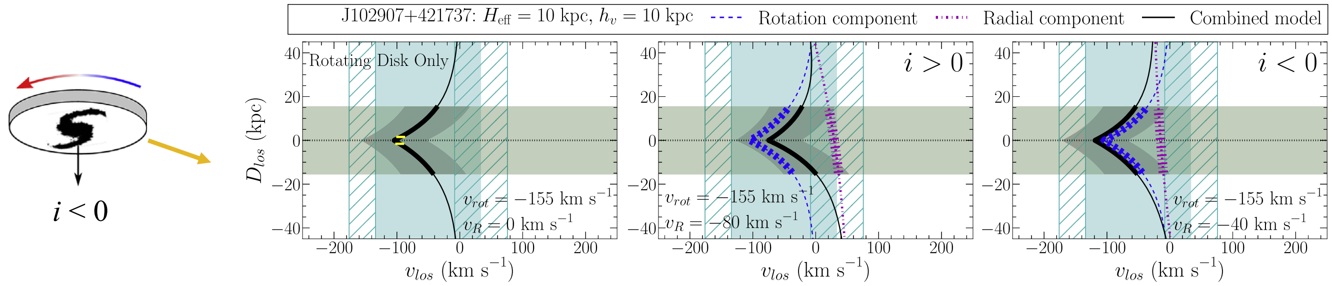

**Figure 6.** J102907+421737: disk tilt tightens constraint on radial inflow speed. The galaxy has a negatively inclined disk (the schematic diagram and Section 3.3.2). A rotating disk (left) of $h_v = 10$ kpc with $H_{\rm eff} = 10$ kpc can reproduce the observed LOS velocity range within measurement uncertainties. A sightline that intersects a thinner disk, e.g., an $H_{\rm eff} = 1$ kpc disk (yellow markers), cannot produce a broad enough velocity range. Disks with positive (middle) and negative (right) inclinations allow maximum radial inflow speeds of 80 and 40 km s$^{-1}$ respectively. Otherwise, the absorption becomes not blue enough or too blue at the disk midplane. With the inferred disk inclination being negative, the radial inflow speed cannot exceed 40 km s$^{-1}$.

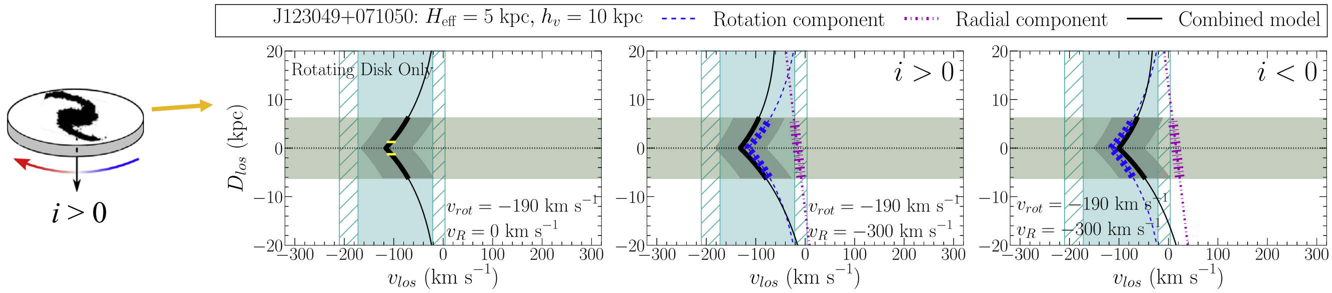

**Figure 7.** J123049+071050: disk tilt cannot tighten constraint on radial inflow speed. We deduce the disk as being positively inclined (the schematic diagram and Section 3.3.3). A rotating disk (left) of $H_{\rm eff} = 5$ kpc and $h_v = 10$ kpc can explain the velocity range of the absorption, and a thinner disk cannot create broad enough absorption with the red absorption end close to the galaxy systemic velocity. Alternatively, regardless of which way the disk tilts, a radial inflow of 300 km s$^{-1}$ changes the velocities at both the blue and the red ends by no more than 20 km s$^{-1}$ (middle and right). Both tilts can still reproduce the measured LOS velocity range within measurement uncertainties. Hence, knowing the disk tilt a priori cannot tighten the constraint on the radial inflow speed.

100 km s$^{-1}$. Therefore, for this galaxy, its negatively inclined disk excludes the detection of radial inflow in the sightline.

## 4. Discussion and Implications

Which way a galaxy disk tilts on the sky can be deduced from the wrapping direction of the spiral arms and the direction of disk rotation (Figures 2 and 3). Using a radial inflow model with gas spiraling inward on the disk plane (as described in Paper I), the four examples in Section 3 have demonstrated incorporating the disk tilt as an extra parameter in modeling the circumgalactic gas kinematics. With a priori knowledge on the disk tilt, our examples show that we can constrain the radial inflow speed for a galaxy or even exclude radial inflow.

### 4.1. The Projection of Radial Inflow is Not Symmetric About a Disk Flip

In the radial inflow model, which way the disk tilts alters the projected LOS velocity from an individual velocity component and results in different LOS velocity ranges. The key to this asymmetry is the location where the sightline intersects the disk tangentially.[10] At this tangent point, the sightline is normal to the radial velocity vector, producing zero LOS velocity. If the disk rotation does not have a vertical velocity gradient, then this tangent point also produces the maximum rotational velocity projection of $v_{\rm rot}$ sin$|i|$. When the disk flips, the tangent point switches from one side to the other side of the disk.[11] This affects whether or not the LOS velocities of the rotation and the inflow components have the same sign near the disk midplane, which determines whether the radial inflow boosts or cancels the projected rotation velocity. Consequently, flipping the disk alters the resultant LOS velocity produced by the two velocity components.

J142459+382113 most clearly demonstrates how this property affects the modeling. As explained in Section 3.3.5, the radial inflow has to cancel the excess blue absorption produced by the disk rotation. To achieve this configuration, this galaxy disk must have a positive inclination; the tangent point is at the far side of the disk ($D_{\rm los} > 0$), so that near the disk midplane, the rotation and radial inflow components produce blue and red Doppler velocities, respectively. However, the disk is negatively inclined, and hence, this rules out the radial inflow detection in this sightline.

### 4.2. Constraining Radial Inflow Speed or Predicting the Disk Tilt

When we use the model to explain the measured LOS velocity range, the observationally deduced disk tilt allows us to constrain the maximum radial inflow speed or exclude radial inflow detection. For example, the observed disk tilt of

---

[10] The sightline intersects the disk tangentially only at the point where the disk radius is equal to the sightline impact parameter $b$. In general, at different $D_{\rm los}$, the sightline intersects the disk at different disk radii larger than $b$.

[11] Whether the tangent point is at the near side or the far side of the disk does not only depend on which way the disk tilts, but also depends on the position of the quasar sightline with respect to the galaxy disk.

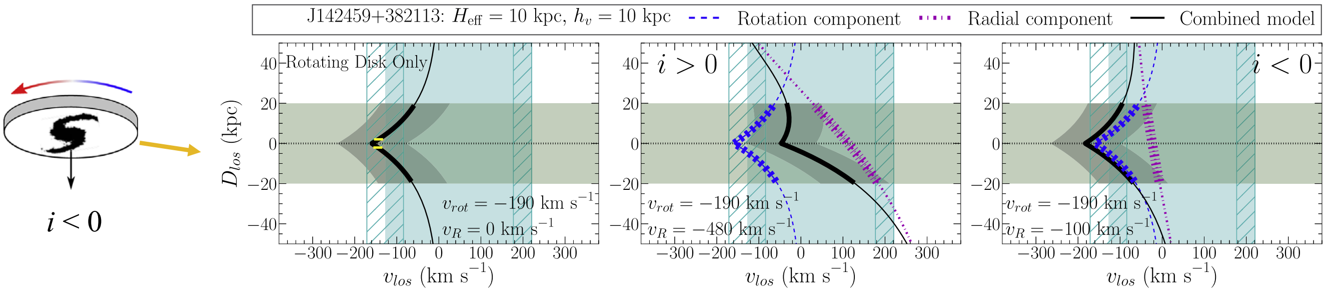

**Figure 8.** J142459+382113: disk tilt excludes radial inflow detection. The disk is negatively inclined (the schematic diagram and Section 3.3.5). Regardless of the thickness of the disk, disk rotation alone (left) cannot reproduce the broad absorption that spans both sides of the galaxy systemic velocity, and the rotation produces bluer absorption near the disk midplane than measured. Only a positively inclined disk (middle) can reproduce the LOS velocity range. However, the disk is negatively inclined. Introducing radial inflow produces even bluer net absorption (right) than a rotating disk (left) near the midplane. We demonstrate this problem using a fiducial inflow speed of 100 km s$^{-1}$. Hence, the negatively inclined disk of this galaxy excludes the detection of radial inflow in the sightline.

J091954+291345 (Figure 5) and J102907+421737 (Figure 6) constrains the inflow speeds to 30–40 km s$^{-1}$, instead of ≈100 km s$^{-1}$ allowed by the opposite tilt. We also exclude radial inflow detection for J142459+382113 (Figure 8), because its disk tilts in a direction opposite to that allowed by the model. Therefore, in principle, we can use the sign of disk inclination as an extra geometrical parameter while modeling the Mg II velocity range along the LOS, and hence, the asymmetry between the disk tilt and LOS velocity measurements helps model the circumgalactic gas kinematics.

However, our example of J123049+071050 has revealed a caveat: not all resultant LOS velocity ranges are sensitive to the radial inflow speed and/or change significantly when we flip the disk (Figure 7). In fact, this example has demonstrated that both the magnitude of the galaxy disk inclination $|i|$ and the azimuthal angle $\alpha$ of the quasar sightline affect whether or not the disk tilt can constrain the radial inflow speed. We consider these two factors separately as follows.

First, since both the rotation and radial inflow velocity vectors lie on the disk plane, a less inclined disk produces a smaller LOS velocity projection. For example, for a face-on ($i = 0°$) disk, because both the tangential (rotation) and radial (inflow) velocity vectors are perpendicular to the sightline, we always detect zero velocity along the LOS. Therefore, due to the projection effect, the LOS velocity and the velocity range of a low-inclination disk are insensitive to the change in the radial inflow speed.

Second, when the $\alpha$ is small, two disks of the same inclination $|i|$ but with opposite tilts produce similar projected LOS velocity from the radial component. The projected radial velocity switches sign where the sightline intersects the disk tangentially, and this tangent point switches sides when the disk flips (Section 4.1). But for an $\alpha = 0°$ sightline, the tangent point is on the disk midplane, hence flipping the disk does not change the projected radial velocity along the LOS. As $\alpha$ increases, the tangent point moves away from the disk midplane. Flipping the disk then changes how the projected radial velocity varies along the LOS, resulting in different resultant LOS velocities and velocity ranges when we combine the radial and rotation velocity components.

In short, a less inclined disk makes the LOS velocity insensitive to the change in the radial inflow speed, and a small azimuthal angle leads to a small difference in the resultant projected LOS velocity between the two disk tilts. Consequently, to use the disk tilt to tighten the constraint on the radial inflow speed, we should avoid configurations that produce the tangent point on or near the disk midplane. Hence, inclined disks should be used, and $\alpha \approx 0°$ sightlines should be avoided.

Since we have observationally deduced how the disk tilts for our galaxies, we use the asymmetry between the tilt and the LOS velocity range to constrain the inflow speed or reject the detection of radial inflow. But even if the disk tilt is not measured a priori, we can use the asymmetry to make a testable prediction on which way the disk tilts if only one of them can reproduce the measured LOS velocity range. For example, the radial inflow modeling for J142459+382113 would predict a positive disk inclination. But because we deduce a negative inclination from the rotation curve and the wrapping direction of the spiral arms, we can then conclude that the sightline does not detect radial inflow on the disk plane.

### 4.3. Radial Inflow Detection and Inside-out Disk Growth

A galaxy disk with a bluer outer disk but a redder inner disk indicates that the outer disk has a younger stellar population (de Jong 1996; Bell & de Jong 2000; MacArthur et al. 2004). While dust can contribute to the color gradient, it is unlikely that the gradient, especially at the outer disk, is largely due to dust extinction (Section 5 of MacArthur et al. 2004). Hence, a bluer outer disk suggests that the disk grows inside-out. For J142459+382113 and J102907+421737, we have obtained images in all F390W, F814W, and $K_s$ bands, and the color images (Figure 4) show the presence of the color gradients. Hence, both disks need a gas supply to grow the disks and fuel the star formation in the outer disks.

However, for J142459+382113, neither a rotating disk nor the radial inflow model can explain the broad velocity range spanned by the Mg II absorption. This suggests that the sightline does not detect radial inflow near the disk plane. A disk growing inside-out but without radial inflow detected may seem contradictory. However, inflow may not need to be axisymmetric, such as the infalling streams seen in simulations (e.g., Nelson et al. 2013; Stewart et al. 2017). Our sightline may simply miss the inflow: both observations and simulations suggest that inflows have a small covering factor. Down-the-barrel spectral observations only identify inflows in a few percent of galaxies (Martin et al. 2012; Rubin et al. 2012), a result consistent with inflow covering a small solid angle, and thereby agrees with simulations that predict a small covering factor for cold accretion streams (e.g., Faucher-Giguère & Kereš 2011; van de Voort & Schaye 2012). Therefore, whether or not we detect radial inflow near the disk plane does not imply the presence or absence of a disk color gradient or inside-out disk growth. Instead, our result possibly informs us about the spatial geometry of the inflowing gas.

On the other hand, for J102907+421737, we have constrained the maximum radial inflow speeds as 40 km s$^{-1}$; hence, the inflow possibly feeds the growing disk. We are also able to constrain the radial inflow speeds for another galaxy, J091954+291345, as 30 km s$^{-1}$. A 30–40 km s$^{-1}$ radial inflow speed is consistent with inflow gas measurements and models of the Milky Way and nearby galaxies. For example, Complex C falls toward the Galactic plane at 50–100 km s$^{-1}$ (Wakker et al. 1999), and the extraplanar H I gas in the Milky Way has shown evidence of infall motion at 20–30 km s$^{-1}$(Marasco & Fraternali 2011). As for nearby galaxies, the H I gas of NGC 2403 moves radially inward at 10–20 km s$^{-1}$ (Fraternali et al. 2002), and the Si IV absorbing gas in M33 has a modeled vertical accretion speed of 110 km s$^{-1}$ at the disk-halo interface (Zheng et al. 2017). In our model, we have only considered infall in the radial direction on the disk plane but not infall perpendicular to the disk plane. Since our sightlines have impact parameters of tens of kiloparsecs instead of a few kiloparsecs as in Zheng et al. (2017), it becomes unphysical if the gas falls toward the extended disk plane at large radii but not toward the central region of the galaxy, where the gravitational potential is the lowest. And because of the corotation between the Mg II gas and the disk rotation (Paper I and M19) and the formation of extended gas disks in simulations (see Introduction), we have modeled radial inflow in the disk plane instead of spherical inflow. We emphasize, however, that although the gas kinematics require the CGM to have a component of angular momentum aligned with that of the disk, they do not directly constrain the location of the absorbing gas along the LOS. Radial inflow in the disk plane is consistent with these constraints, but other solutions may be possible, e.g., satellites accreting onto the galaxy (Shao et al. 2018), series of gas clouds intercepted by the sightline but not all clouds are spiraling toward the galaxy, etc. Our simple radial inflow model predicts inflow speeds that are at least consistent with measurements for the Milky Way and nearby galaxies.

## 5. Conclusion

In this paper, we determined the 3D orientation of galactic disks to constrain circumgalactic gas flow models. We presented new images from Keck/NIRC2 (with LGSAO) and *HST*/WFC3 to determine the orientation of galaxy disks on the sky. Since spiral arms trail the direction of rotation, the rotation curve measurements and the wrapping direction of spiral arms reveal the disk orientation in 3D space, i.e., the 3D disk orientation (Figures 2 and 3).

We modeled the Mg II gas kinematics measured at four quasar sightlines around $z \approx 0.2$, star-forming galaxies. We selected the galaxy–quasar pairs from Paper I and M19, and all sightlines intersect the inner CGM and lie within 30° from the galaxy major axes. We used the new galaxy images and the rotation curve measurements to determine the 3D disk orientation of these galaxies. Together with our inflow model with gas spiraling inward in the disk plane, we modeled the broad LOS velocity range spanned by the Mg II absorption, for which the broad velocity ranges are known to pose challenges in kinematic modeling.

Combining our radial inflow model and the measured disk tilt can constrain the inflow speed or rule out radial inflow detection. We constrained the maximum radial inflow speeds for two galaxies as 30–40 km s$^{-1}$, consistent with inflow measurements for the Milky Way and nearby galaxies. On the other hand, we excluded the detection of radial inflowing gas in the sightline of one galaxy, because the disk tilts in a direction opposite to that permitted by the model.

The inflow speeds constrained by our model are also observed in simulations. The inferred inflow speeds agree with those for galaxies of similar masses in the `EAGLE` simulations; the comparable mass inflow rates (order of unity in $M_\odot$ yr$^{-1}$) and galaxy star formation rates suggest that the inflowing gas plausibly sustains the galaxy star-forming activities (Ho et al. 2019), and the gas precesses and aligns its angular momentum vector with the preexisting cold gas in the galactic disk (Stevens et al. 2017). Low-redshift, Milky Way–like galaxies in the `FIRE` simulations also show order-of-unity mass inflow rates in total, which include the contribution from distinct sources of materials growing the galaxy, e.g., fresh accretion from the intergalactic medium, accretion of wind materials expelled by the galaxies themselves and/or the gas exchange between galaxies via winds (Muratov et al. 2015; Anglés-Alcázar et al. 2017).

The bluer outer disks of our galaxies indicate that the outer disks are younger, consistent with disks growing inside-out. This may seem at odds with not detecting radial inflow for the one galaxy. However, the galaxy disk may accrete gas from infalling streams, but our sightline has not fortuitously intersected the streams due to their small covering factor. The “nondetection” thereby informs us about the spatial geometry and the distribution of the feeding gas.

One of our examples demonstrated that the disk inclination angle and the azimuthal angle of the quasar sightline also affect whether the disk tilt can effectively constrain the radial inflow speed. Typically, we can constrain or rule out radial inflow because flipping the disk changes how the radial and rotation velocity vectors add together, producing different LOS velocities and velocity ranges. However, for a less inclined disk, the projected LOS velocity becomes insensitive to the variation of the radial inflow speed. And for a sightline at small azimuthal angle, because the tangent point lies near the disk midplane, the two disk tilts produce LOS velocities that are hardly distinguishable. Hence, in the future, to search for and model radial inflow on the galactic disk plane, observers should select inclined disks and avoid $\alpha \approx 0°$ sightlines.

We thank the referee for thoughtful comments and suggestions that improved the organization of the manuscript. This research was supported by Space Telescope Science Institute under grant HST-GO-14754.001-A and the National Science Foundation under AST-1817125. The rotation curve data used here were obtained at the Apache Point Observatory (APO) 3.5 m telescope, which is owned and operated by the Astrophysical Research Consortium. Observing time was allocated to the New Mexico State University through Chris Churchill, who is supported by the National Science Foundation under AST-1517816. These APO data were previously published in Paper I and M19, and we gratefully acknowledge the contributions of Chris Churchill and Glenn Kacprzak to the rotation curve data. Some of the data used herein were obtained at the W. M. Keck Observatory, which is operated as a scientific partnership among the California Institute of Technology, the University of California and the National

Aeronautics and Space Administration. The Observatory was made possible by the generous financial support of the W. M. Keck Foundation. The authors wish to recognize and acknowledge the very significant cultural role and reverence that the summit of Maunakea has always had within the indigenous Hawaiian community. We are most fortunate to have the opportunity to conduct observations from this mountain.

*Facilities: HST* (WFC3), Keck:II (NIRC2), Keck:I (LRIS), ARC (DIS).

## ORCID iDs

Stephanie H. Ho https://orcid.org/0000-0002-9607-7365
Crystal L. Martin https://orcid.org/0000-0001-9189-7818

## References

Anglés-Alcázar, D., Faucher-Giguère, C.-A., Kereš, D., et al. 2017, MNRAS, 470, 4698
Barcons, X., Lanzettat, K. M., & Webb, J. K. 1995, Natur, 376, 321
Bell, E. F., & de Jong, R. S. 2000, MNRAS, 312, 497
Benjamin, R. A. 2002, in ASP Conf. Ser. 276, Seeing Through the Dust: The Detection of HI and the Exploration of the ISM in Galaxies, ed. A. R. Taylor, T. L. Landecker, & A. G. Willis (San Francisco, CA: ASP), 201
Bigiel, F., Leroy, A., Walter, F., et al. 2008, AJ, 136, 2846
Bigiel, F., Leroy, A. K., Walter, F., et al. 2011, ApJL, 730, L13
Bordoloi, R., Lilly, S. J., Knobel, C., et al. 2011, ApJ, 743, 10
Bouché, N., Finley, H., Schroetter, I., et al. 2016, ApJ, 820, 121
Bouché, N., Hohensee, W., Vargas, R., et al. 2012, MNRAS, 426, 801
Bouché, N., Murphy, M. T., Kacprzak, G. G., et al. 2013, Sci, 341, 50
Brook, C. B., Stinson, G., Gibson, B. K., Wadsley, J., & Quinn, T. 2012, MNRAS, 424, 1275
Carlberg, R. G., & Freedman, W. L. 1985, ApJ, 298, 486
Chen, H.-W., Kennicutt, R. C., Jr., & Rauch, M. 2005, ApJ, 620, 703
Chen, H.-W., & Mulchaey, J. S. 2009, ApJ, 701, 1219
Christensen, C. R., Davé, R., Governato, F., et al. 2016, ApJ, 824, 57
Danovich, M., Dekel, A., Hahn, O., Ceverino, D., & Primack, J. 2015, MNRAS, 449, 2087
Danovich, M., Dekel, A., Hahn, O., & Teyssier, R. 2012, MNRAS, 422, 1732
de Jong, R. S. 1996, A&A, 313, 377
El-Badry, K., Quataert, E., Wetzel, A., et al. 2018, MNRAS, 473, 1930
Faucher-Giguère, C.-A., & Kereš, D. 2011, MNRAS, 412, L118
Ford, A. B., Davé, R., Oppenheimer, B. D., et al. 2014, MNRAS, 444, 1260
Fraternali, F., van Moorsel, G., Sancisi, R., & Oosterloo, T. 2002, AJ, 123, 3124
Fruchter, A. S., Hack, W., Dencheva, N., Droettboom, M., & Greenfield, P. 2010, in BetaDrizzle: A Redesign of the MultiDrizzle Package, Space Telescope Science Institute Calibration Workshop, ed. S. Deustua & C. Oliveira, 382
Gentile, G., Józsa, G. I. G., Serra, P., et al. 2013, A&A, 554, A125
Ghez, A. M., Salim, S., Weinberg, N. N., et al. 2008, ApJ, 689, 1044
Gonzaga, S., et al. 2012, The DrizzlePac Handbook (Baltimore, MD: STScI)
Heckman, T., Borthakur, S., Wild, V., Schiminovich, D., & Bordoloi, R. 2017, ApJ, 846, 151
Ho, S. H., Martin, C. L., Kacprzak, G. G., & Churchill, C. W. 2017, ApJ, 835, 267
Ho, S. H., Martin, C. L., & Turner, M. L. 2019, ApJ, 875, 54
Johnson, S. D., Chen, H.-W., & Mulchaey, J. S. 2013, MNRAS, 434, 1765
Johnson, S. D., Chen, H.-W., & Mulchaey, J. S. 2015, MNRAS, 449, 3263
Kacprzak, G. G., Churchill, C. W., Barton, E. J., & Cooke, J. 2011, ApJ, 733, 105
Kacprzak, G. G., Churchill, C. W., Ceverino, D., et al. 2010, ApJ, 711, 533
Kacprzak, G. G., Churchill, C. W., & Nielsen, N. M. 2012, ApJL, 760, L7
Kacprzak, G. G., Muzahid, S., Churchill, C. W., Nielsen, N. M., & Charlton, J. C. 2015, ApJ, 815, 22
Kamphuis, P., Rand, R. J., Józsa, G. I. G., et al. 2013, MNRAS, 434, 2069
Kennicutt, R. C., Jr. 1983, ApJ, 272, 54
Kennicutt, R. C., Jr. 1998, ARA&A, 36, 189
Kimm, T., Devriendt, J., Slyz, A., et al. 2011, arXiv:1106.0538
Krist, J. E., Hook, R. N., & Stoehr, F. 2011, Proc. SPIE, 8127, 81270J
Lagos, C. d. P., Theuns, T., Stevens, A. R. H., et al. 2017, MNRAS, 464, 3850
Leroy, A. K., Walter, F., Brinks, E., et al. 2008, AJ, 136, 2782
Leroy, A. K., Walter, F., Sandstrom, K., et al. 2013, AJ, 146, 19
MacArthur, L. A., Courteau, S., Bell, E., & Holtzman, J. A. 2004, ApJS, 152, 175
Marasco, A., & Fraternali, F. 2011, A&A, 525, A134
Martin, C. L., Ho, S. H., Kacprzak, G. G., & Churchill, C. W. 2019, ApJ, 878, 84
Martin, C. L., Shapley, A. E., Coil, A. L., et al. 2012, ApJ, 760, 127
Muratov, A. L., Kereš, D., Faucher-Giguère, C.-A., et al. 2015, MNRAS, 454, 2691
Nelson, D., Vogelsberger, M., Genel, S., et al. 2013, MNRAS, 429, 3353
Nielsen, N. M., Churchill, C. W., Kacprzak, G. G., Murphy, M. T., & Evans, J. L. 2015, ApJ, 812, 83
Nielsen, N. M., Kacprzak, G. G., Pointon, S. K., Churchill, C. W., & Murphy, M. T. 2018, ApJ, 869, 153
Oke, J. B., Cohen, J. G., Carr, M., et al. 1995, PASP, 107, 375
Oosterloo, T., Fraternali, F., & Sancisi, R. 2007, AJ, 134, 1019
Oppenheimer, B. D., Davé, R., Kereš, D., et al. 2010, MNRAS, 406, 2325
Peng, C. Y., Ho, L. C., Impey, C. D., & Rix, H.-W. 2002, AJ, 124, 266
Pichon, C., Pogosyan, D., Kimm, T., et al. 2011, MNRAS, 418, 2493
Planck Collaboration, Ade, P. A. R., Aghanim, N., et al. 2016, A&A, 594, A13
Prochaska, J. X., & Wolfe, A. M. 1997, ApJ, 487, 73
Putman, M. E., Peek, J. E. G., & Joung, M. R. 2012, ARA&A, 50, 491
Rahman, N., Bolatto, A. D., Xue, R., et al. 2012, ApJ, 745, 183
Rockosi, C., Stover, R., Kibrick, R., et al. 2010, Proc. SPIE, 7735, 77350R
Rubin, K. H. R., Prochaska, J. X., Koo, D. C., & Phillips, A. C. 2012, ApJL, 747, L26
Schmidt, M. 1963, ApJ, 137, 758
Shao, S., Cautun, M., Frenk, C. S., et al. 2018, MNRAS, 476, 1796
Shen, S., Madau, P., Aguirre, A., et al. 2012, ApJ, 760, 50
Sommer-Larsen, J. 1991, MNRAS, 249, 368
Steidel, C. C., Kollmeier, J. A., Shapley, A. E., et al. 2002, ApJ, 570, 526
Stevens, A. R. H., Lagos, C. d. P., Contreras, S., et al. 2017, MNRAS, 467, 2066
Stewart, K. R., Brooks, A. M., Bullock, J. S., et al. 2013, ApJ, 769, 74
Stewart, K. R., Kaufmann, T., Bullock, J. S., et al. 2011, ApJ, 738, 39
Stewart, K. R., Maller, A. H., Oñorbe, J., et al. 2017, ApJ, 843, 47
Tumlinson, J., Peeples, M. S., & Werk, J. K. 2017, ARA&A, 55, 389
van Dam, M. A., Bouchez, A. H., Le Mignant, D., et al. 2006, PASP, 118, 310
van de Voort, F., & Schaye, J. 2012, MNRAS, 423, 2991
van den Bergh, S. 1962, AJ, 67, 486
van Dokkum, P. G. 2001, PASP, 113, 1420
Wakker, B. P., Howk, J. C., Savage, B. D., et al. 1999, Natur, 402, 388
Werk, J. K., Prochaska, J. X., Tumlinson, J., et al. 2014, ApJ, 792, 8
Wizinowich, P. L., Le Mignant, D., Bouchez, A. H., et al. 2006, PASP, 118, 297
Worthey, G., Dorman, B., & Jones, L. A. 1996, AJ, 112, 948
Zabl, J., Bouché, N. F., Schroetter, I., et al. 2019, MNRAS, 485, 1961
Zheng, Y., Peek, J. E. G., Werk, J. K., & Putman, M. E. 2017, ApJ, 834, 179
Zschaechner, L. K., Rand, R. J., Heald, G. H., Gentile, G., & Józsa, G. 2012, ApJ, 760, 37
Zschaechner, L. K., Rand, R. J., Heald, G. H., Gentile, G., & Kamphuis, P. 2011, ApJ, 740, 35